Numerical modeling and observations of seismo-acoustic waves propagating as modes in a fluid-solid waveguide

Jean Lecoulant, Claude Guennou, Laurent Guillon, Jean-Yves Royer

JASA ARTICLE

Numerical modeling and observations of seismo-acoustic waves propagating as modes in a fluid-solid waveguide

Jean Lecoulant,[1,a)] Claude Guennou,[1] Laurent Guillon,[2] and Jean-Yves Royer[1]
[1]*Laboratoire Géosciences Océan, University of Brest & CNRS, 1 rue Dumont d'Urville, 29280 Plouzané, France*
[2]*Institut de Recherche de l'École Navale, CC 600, 29240 Brest Cedex 9, France*

ABSTRACT:
This paper discusses the nature of the low-frequency seismo-acoustic waves generated by submarine earthquakes in the ocean. In a finite-depth homogeneous ocean over a semi-infinite solid crust, the derivation of the acoustic equations shows that waves propagate as modes. The waves propagating with the speed of sound in water (T waves) are preceded by waves with frequencies below the Airy phase. Furthermore, the group speeds of these modes are sensitive to the environmental setting. As a test, we applied the spectral finite-element code SPECFEM2D in a simplified configuration with an ocean layer overlaying a solid crust, and a seismic source below a Gaussian seamount surrounded by a flat seafloor. The simulations confirm that the generated T waves and their precursors follow the theoretical dispersion curves. A more realistic environment with a seismically-layered crust and a sound-speed profile in the ocean is then used to predict the expected acoustic modes. Although noisy, recordings by ocean bottom seismometers from the southwest Indian Ocean show T waves preceded by ultra-low frequency waves, which display two modes comparable to the theoretical ones. They are in good agreement for mode 1, whereas, for mode 0, a slight offset in frequency has yet to be explained. © *2022 Acoustical Society of America*. https://doi.org/10.1121/10.0010529

(Received 13 April 2021; revised 19 April 2022; accepted 22 April 2022; published online 25 May 2022)
[Editor: Ying-Tsong Lin] Pages: 3437–3447

I. INTRODUCTION

Seismic waves generated by underwater seismic activity are converted at the sea bottom into seismo-acoustic waves. Among them, T waves propagate horizontally, at the speed of sound, in the water column, over very long distances (∼ 1000 km) with low attenuation. They may also preserve near-field and high-frequency (compared to seismic waves) information lost otherwise because of the strong seismic attenuation in the crust. T waves are therefore of great interest for monitoring underwater seismic activity in oceanic regions remote from terrestrial seismometer arrays. Arrival times of T waves are routinely exploited through trilateration to locate epicenters (e.g., Fox *et al.*, 2001; Johnson, 1966), often assimilated to the source of T waves. Notable efforts have been attempted to extract other information from T-wave signals, such as the source depth from the rise time between first arrivals and the maximal amplitude of T waves (Schreiner *et al.*, 1995), or the source magnitude and focal mechanism from T-wave energy (Dziak, 2001). However, all those observables are sensitive to the way T waves are generated and propagate, which justifies a better understanding of their nature.

Understanding the ocean/crust interactions generating T waves and their interesting properties has led to the development of several models. These waves, first recorded by land-based seismometers, were correctly interpreted as acoustic waves propagating in the ocean (Tolstoy and Ewing, 1950). Press *et al.* (1950) and Biot (1952) applied the modal formalism developed by Pekeris (1948) to T waves and described them as normal modes in a fluid layer over a semi-infinite solid. Following this model, Ewing *et al.* (1957) correctly predicted the dispersion of teleseismic T waves. For mathematical simplicity, their analytical model was derived with a flat bottom. However, in such a situation, seismic waves can hardly be converted into acoustic waves propagating horizontally in the ocean, as pointed out by Ewing *et al.* (1950), who provided theoretical and empirical arguments highlighting the importance of slopes in the generation of T waves. The role of slopes led to the development of a simple and purely geometrical *downslope propagation* model (Johnson *et al.*, 1963; Officer, 1958), using ray tracing based on Snell's law to predict the position of the hypocenter (Milne, 1959) or the distance between the hypocenter and the zone where T waves are converted (Talandier and Okal, 1998). The discovery of abyssal T waves led to non-geometrical models, where T waves would result from wave scattering, initially thought to be due to the sea-surface roughness (Johnson *et al.*, 1968) but more likely to the seafloor roughness (Fox *et al.*, 1994). Park *et al.* (2001) showed that T waves result from the coupling along the fluid-solid interface between high-order modes excited by the seismic source and low-order modes propagating acoustic energy horizontally in the ocean. Mode coupling jointly explains downslope propagation and scattering from a rough sea bottom since both a slope or a rough interface breaks the mode orthogonality. Park *et al.* (2001) considered

[a)]Also at: Institut de Recherche de l'École Navale, CC 600, 29240 Brest Cedex 9, France. Electronic mail: jean.lecoulant@univ-brest.fr

modes in a fluid-solid waveguide (with shear in the sea bottom), including fundamental mode 0 (labelled as the Stoneley mode). The modal content of observed T waves was demonstrated by D'Spain *et al.* (2001) who compared actual spectrograms from a 3000 m-long and 200-hydrophone vertical array, to simulated modes (using the code KRAKEN; Porter, 1991). In the presence of an important layer of sediments, Butler and Lomnitz (2002) observed a banded modal structure of T waves and attributed it to modes in a fluid-solid waveguide (labelled as Rayleigh modes). More recently, Bottero (2018) pointed out several observations that can only be explained if T waves propagate as modes.

Progress in computing resources made it possible to simulate T waves in realistic configurations, enabling direct comparisons with real data, where deriving exact analytical solutions would be difficult. Piserchia *et al.* (1998) used a two-dimensional (2D) hybrid model combining ray-tracing with finite-elements to reproduce T waves generated by a chemical blast, with a focus on the retro-conversion from acoustic to seismic waves on an atoll slopes. The theory based on modal scattering made it possible to model T waves in a three-dimensional (3D) configuration and was able to predict the envelope (de Groot-Hedlin and Orcutt, 1999) and the spectrogram (de Groot-Hedlin and Orcutt, 2001) of T waves from real events. The method was later improved by Yang and Forsyth (2003) to include the excitation of T waves by S waves. They noted that the relatively simple computation of modal scattering was a good alternative to computationally intensive finite-element modeling of T waves. Yet, Jamet *et al.* (2013), Bottero (2018), and Stevens *et al.* (2020) achieved simulating T waves in their complete waveform with a 2D finite-element code (SPECFEM2D; Cristini and Komatitsch, 2012; Tromp *et al.*, 2008); these simulations outlined the modal nature, particularly the modal dispersion of the predicted T waves. With a similar approach (SPECFEM3D), Lecoulant *et al.* (2019) investigated 3D-effects on the generation and propagation of T waves and noted that they propagate as modes in a fluid-solid waveguide (labelled as Rayleigh modes). Parabolic equations were also used to simulate T-wave conversion in 2D idealized configurations (Franck *et al.*, 2015). Oliveira and Lin (2019) demonstrated the relevance of this approach to compute transmission losses of T waves at a given frequency, over distances of thousands kilometers and taking into account the seafloor bathymetry. Ray tracing was also used to simulate T waves (Chen *et al.*, 2017).

This brief review of the state-of-the-art reflects the general acceptance of the modal propagation of T waves. However, the dispersion curves expected if they propagate as modes in a fluid-solid waveguide have been scarcely discussed since the seminal articles on the question in the 1950s (Biot, 1952; Ewing *et al.*, 1957; Press *et al.*, 1950). To our knowledge, only Ewing *et al.* (1957) and Butler and Lomnitz (2002) proposed experimental evidence that T waves propagate as such modes. To fill this gap, this article attempts to re-examine the issue using theoretical, numerical, and experimental evidence. We present a method to derive the group speeds of the modes in a fluid-solid waveguide, briefly study their sensitivity to the environmental parameters in the crust and the ocean, and discuss the modal signature expected in spectrograms of seismo-acoustic waves (Sec. II). We then use SPECFEM2D to explore the effects of the source frequency of velocity-layered crust and water column and of the wave attenuation in the crust (Sec. III), which are difficult to account for in an analytical demonstration. In spite of its large numerical cost, this finite-element code is among the few models that can generate a complete waveform comparable to real data, based on a seismic source in the crust, with no intrinsic limitation in its frequency range and a range-dependent environment. Finally, we provide spectrograms of observed T waves preceded by waves propagating as modes, generated by an actual earthquake in 2013 and recorded by ocean bottom seismometers (OBSs) and discuss the agreement of observed modes with theoretical modes (Sec. IV).

II. SEISMO-ACOUSTIC WAVES AS MODES IN A FLUID-SOLID WAVEGUIDE

A. Numerical resolution of the dispersion relation

The classical derivation by Tolstoy and Ewing (1950), Press *et al.* (1950), or Biot (1952) describes the propagation of modes in an ocean with a finite depth h overlying a semi-infinite elastic solid with a shear velocity higher than the water sound-speed. For an ocean with a flat-bottom, the theory can be derived in two dimensions without loss of generality due to the cylindrical symmetry. The fluid layer, the ocean, is defined by its mean density ρ_w and sound speed c_w. The semi-infinite elastic solid is defined by its mean density ρ_s, the speed of pressure waves (P waves) c_P, and the speed of shear waves (S waves) c_S.

Injecting the solutions of the linearized wave equation of circular frequency ω and wavenumber K in the four boundary conditions:

- a null acoustic pressure at the sea surface
- a null tangential stress at the sea bottom
- the continuity of the normal speed at th sea bottom
- the continuity of the normal stress at the sea bottom

lead to the classical dispersion relation (Stoneley, 1926),

$$\tan(lh) = \frac{l\rho_s}{m\rho_w}\frac{4c_S^4K^2mn - (\omega^2 - 2K^2c_S^2)^2}{\omega^4}, \tag{1}$$

with the vertical wavenumbers,

$$l = \sqrt{\frac{\omega^2}{c_w^2} - K^2}, \quad m = \sqrt{K^2 - \frac{\omega^2}{c_P^2}}, \quad n = \sqrt{K^2 - \frac{\omega^2}{c_S^2}}. \tag{2}$$

For $\omega/c_S \leq K < \omega/c_w$, the three vertical wavenumbers l, m, and n are real and, therefore, both members of Eq. (1) are real. For $K = \omega/c_w$, $l = 0$ and the acoustic pressure is identically null in the water column. For $K > \omega/c_w$, l is

https://doi.org/10.1121/10.0010529

imaginary, m and n are real and, therefore, both members of Eq. (1) are imaginary. Searching for zeros of Eq. (1) is eased since only the real part of the equation needs to be considered below $K = \omega/c_w$ and only the imaginary part of the equation needs to be considered above $K = \omega/c_w$.

For the numerical applications, we chose typical parameters for the ocean and the crust (Searle, 2013) (Table I). Figure 1 displays the resulting left- and right-hand members of Eq. (1) for a low frequency (0.25 Hz), at which the limited number of modes makes the situation easy to visualize. At this frequency, Eq. (1) has two solutions corresponding to mode 0 ($K = K_0$) and mode 1 ($K = K_1$), with $K_1 < K_0 < \omega/c_w$. There is no solution for $K > \omega/c_w$.

As noticed by Ball *et al.* (2016), an analytical solution exists for the dispersion relation 1, but its numerical solution is much easier to calculate. When wavenumbers K of all modes existing in the frequency domain of interest are known, the group speed of each mode can be easily deduced. To do so, the circular frequency must be derivated with respect to the wavenumber along each mode, by approximating $\partial\omega/\partial K$ by ratios of circular frequency differences over wavenumber differences. The forward finite-difference scheme shows no numerical noise for the frequency step (10^{-3} Hz) and the wavenumber step (5×10^{-9} m^{-1}) used for Fig. 2.

Mode 0 is the solution to Eq. (1) with the lowest frequency and has no cut-off frequency. When f tends to zero, the ocean depth is negligible compared to an infinite wavelength and propagating waves are the interface waves at a vacuum-solid interface: Rayleigh waves. With the parameters in Table I the phase speed and group speed are equal to $c_R = 2736\,\mathrm{m\,s^{-1}}$. The phase and group speed decrease with frequency until the group speed reaches a minimum for $f = 0.165 \pm 0.002$ Hz (Airy phase, reduced frequency $fh/c_w = 0.33 \pm 0.01$) and then increases toward c_w. The phase speed falls below c_w at $f = 1.034 \pm 0.001$ Hz ($fh/c_w = 2.068 \pm 0.002$). For large frequencies, the propagating wavelengths are small and the ocean can be assimilated to a semi-infinite fluid layer. Propagating waves are the interface waves at an interface between a liquid half-space and a solid half-space: Scholte waves. Therefore, with the parameters in Table I, the phase speeds of the modes tend for large frequencies towards 1496 m s^{-1} (Vinh, 2013). Modes other than mode 0 have a cut-off frequency for $c_\phi = c_S$. Their phase speeds decrease monotonously with increasing frequency from $c_\phi = c_S$ to $c_\phi = c_w$ with an inflection point at $c_\phi = c_R$. Their group speeds fall rapidly from $c_g = c_S$ at the cut-off frequency (Ewing *et al.*, 1957) to a local minimum, before

TABLE I. Parameters used to calculate the speeds of theoretical modes.

	h (m)	3000
Ocean	c_w (m s^{-1})	1500
	ρ_w (kg m^3)	1000
	c_P (m s^{-1})	5000
Crust	c_S (m s^{-1})	3000
	ρ_s (kg m^3)	3200

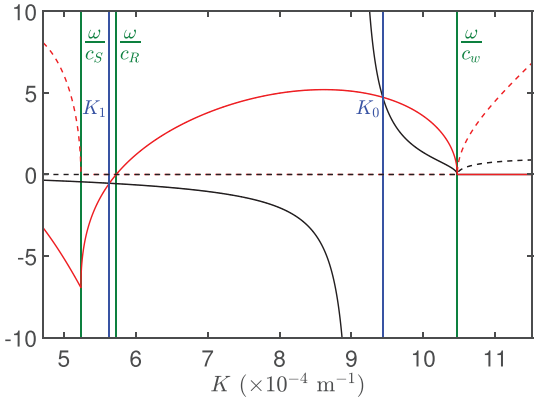

FIG. 1. (Color online) Wavenumbers of the modal solutions of Eq. (1) for the frequency $f = 0.25$ Hz (i.e., $fh/c_w = 0.5$). The right-hand member of Eq. (1) is plotted in red and the left-hand member $\tan(lh)$ in black. The real part of each member of the equation is represented by the solid line and the imaginary part by the dashed line. The annotated blue lines show the two wavenumbers that verify Eq. (1) and the annotated green lines the wavenumbers corresponding to the phase speeds c_S, c_R, and c_w. Physical parameters are from Table I.

increasing again toward a local maximum for a phase speed $c_\phi > c_R$. They then decrease until a minimum at the Airy phase and finally increase towards c_w. The value of the local maximum of the group speed for $c_\phi > c_R$ decreases with increasing mode order and falls below c_w for mode 13 at $f = 3.9$ Hz ($fh/c_w = 7.7$). The minimum of the group speed also decreases with increasing mode order.

If T waves propagate as modes in a fluid-solid waveguide, the arrival of modes below the Airy phase should be observed before T waves, given their group speeds higher than the sound speed, and up to the speed of Rayleigh waves in mode 0. However, the local maximum of the group speeds above the cut-off frequency decreases with increasing mode order. For modes higher than mode 13, the largest

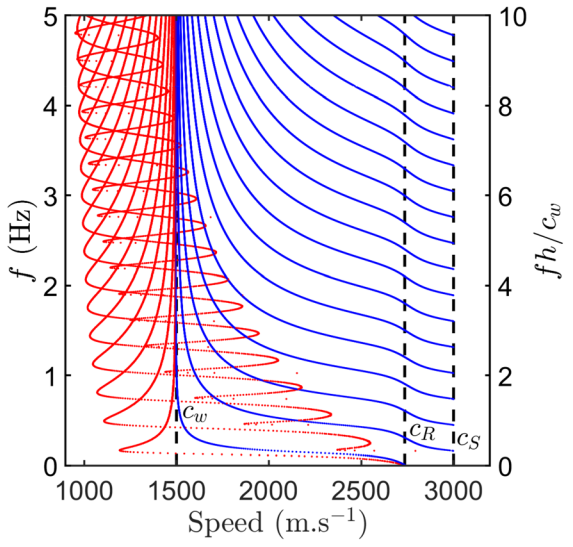

FIG. 2. (Color online) Phase (blue) and group (red) speeds of the 18 first modes vs frequency. Dashed lines show the speeds of acoustic waves in water (c_w), Rayleigh waves without an ocean (c_R), and S waves (c_S). Physical parameters are given in Table I.

part of the modes below the Airy phase travel at a speed smaller than c_w and hence will be indistinguishable from the acoustic waves carried by lower order modes (Fig. 2). Therefore, with the parameters in Table I, the modes below their Airy phase are mixed with the acoustic waves for a frequency higher than 3.9 Hz. The general focus on frequencies higher than 5 Hz in T waves could hence be the reason why precursory ultra-low-frequency waves carried by the part of the modes below the Airy phase remain unnoticed, explaining the lack of evidence for T waves propagating as modes in a fluid-solid waveguide.

B. Sensitivity study

Biot (1952) explored the dependency of the speeds of modes on the parameters in Eq. (1) (h, c_w, c_P, c_S, ρ_w, and ρ_s) and focused on asymptotic values. In the following brief sensitivity study, we explore, among these parameters and within their range in real environments, which cause the largest variation in the speeds of modes, and thus, which are the most influential for predicting modes in unknown environments.

The variation due to h can be easily apprehended through the reduced frequency fh/c_w. Indeed, for fixed ratios c_w/c_P, c_S/c_P, and ρ_w/ρ_s, the group speeds of the modes are invariant over fh/c_w (Biot, 1952). For example, for the modes 0 and 1 calculated with the parameters in Table I, except for $h = 6000$ m, the group speeds will be the same as with $h = 3000$ m but at half the frequency (Fig. 3). In contrast, changes in c_w will modify the limit of the group speeds for high frequencies, and changes in c_S and c_P imply nonlinear changes in the group speeds of modes. However, for changes in c_w while keeping c_S/c_P and ρ_w/ρ_s constant, the Airy phases still occur for the same fh/c_w (0.33 for mode 0 and 1.0 for mode 1, with values in Table I), even if with different group speeds. The speeds of the Airy phases increase with increasing c_w but the maxima of the group speeds

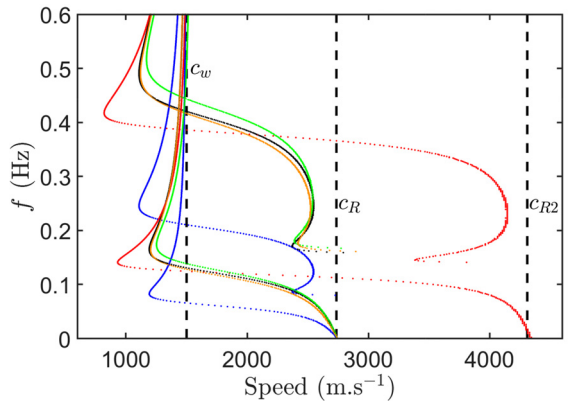

FIG. 3. (Color online) Group speeds of the first two modes vs frequency: in black, calculated with the physical parameters in Table I; in blue, with the parameters in Table I, but an ocean depth of $h = 6000$ m; in green, with the same parameters but a different sound-speed ($c_w = 1550$ m s^{-1}); in red, with the parameters in Table I, but different seismic velocities in the crust ($c_P = 8100$ m s^{-1}, $c_S = 4700$ m s^{-1}, $c_{R2} = 4310$ m s^{-1}); and in orange, with the parameters in Table I, but a crust of density $\rho_S = 2700$ kg m^{-3}.

decrease. With $c_P = 8100$ m s^{-1} and $c_S = 4700$ m s^{-1}, which are typical velocities of seismic waves at the top of the Earth mantle, the highest speed of Rayleigh waves ($c_{R2} = 4310$ m s^{-1}) imposes a higher maximal group speed of mode 0, while the local maximum of the mode 1 above the cut-off frequency is also higher. The cut-off frequencies and those local maxima occur for lower frequencies, as well as the Airy phases that also show lower speeds. With $\rho_s = 2700$ kg m^{-3}, the maximum of the group speeds is slightly lower and the minimum of the group speed slightly higher than with $\rho_s = 3200$ kg m^{-3}.

This brief sensitivity study will help adjust parameters controlling the speeds of the modes in a real and partly unknown environment. Particularly, it points to c_P and c_S as the most critical parameters for predicting the dispersion curves of the modes. The water depth h is generally well known and the other parameters (c_w, ρ_w, and ρ_s) vary within a limited range, so have a lesser effect on the speeds of modes.

III. NUMERICAL MODELING

The aim of this section is to simulate seismo-acoustic waves at a regional scale in a simple configuration to show that they propagate as modes in a fluid-solid waveguide. After this validation, more realistic environments will be tested by adding successively intrinsic attenuation at the sea bottom, a velocity-layered solid crust, and a Sound Fixing and Ranging (SOFAR) channel in the ocean. Though idealized, these simulations help to understand the modal propagation of seismo-acoustic waves in realistic environments and to interpret real data presented in Sec. IV.

A. Parameters

The code SPECFEM2D is run on a 440 km wide (–20 km $\leq x \leq$ 420 km) and 10 km thick (–10 km $\leq z \leq$ 0 km) domain, divided vertically between a 3000 m-deep fluid medium (the ocean) and a 7 km-thick solid medium (the crust). With a perfectly matched absorbing layer (PML) (Xie *et al.*, 2016) at its bottom, the crust can be considered a semi-infinite medium, while similar PMLs at the two vertical sides ($x = -20$ km and $x = 420$ km) avoid spurious reflections. To ensure a mode coupling enabling the generation of T waves (Park *et al.*, 2001), a 2000 m-high seamount, with a Gaussian shape and a 9 km half-width at half-depth, is placed above the source at $x = 0$ km. Away from this seamount, the fluid-solid interface is flat. In Sec. III B, the density and velocity parameters in both media are constant and set to the values given in Table I. In Sec. III C, the solid crust is divided in three homogeneous horizontal layers with increasing densities and velocities of P and S waves, taken from Bassin (2000) (Table II).

A first simulation is performed with physical parameters identical to the ones presented in Table I and no attenuation in the solid crust (Configuration 1) to test the adequation of simulated modes with theoretical modes in the most idealized case. Then, an intrinsic attenuation is taken into account in the solid crust with the parameters

https://doi.org/10.1121/10.0010529

TABLE II. Parameters of the three-layered crust used in Sec. III C.

	Thickness (m)	ρ (kg m^{-3})	c_P (m s^{-1})	c_S (m s^{-1})
Layer 1	1700	2700	5000	3000
Layer 2	2300	2900	6700	3600
Layer 3	3000	3000	7000	3900

$\alpha_P = 0.1\,\mathrm{dB}/\lambda$ for P waves and $\alpha_S = 0.2\,\mathrm{dB}/\lambda$ for S waves (Configuration 2), as for other configurations described below. In Configuration 3, the homogeneous crust is replaced by the three-layered crust described in Table II. Then, a sound-speed profile including a SOFAR channel is used in the ocean. This profile (Fig. 4, top) from Dushaw (2011) is based on the WOA09 (NOAA, 2015) database and was extracted for the location (27° 30′ S; 65° 30′ E) and season (March 2013) of the earthquake studied in Sec. IV. The original 13-layer profile was spline interpolated to a 10 m vertical resolution. Since a SOFAR channel may have more important effects in a deeper ocean, simulations are performed for different water depths: 3000 m (Configuration 4a), 3640 m (Configuration 4b), and 5430 m (Configuration 4c). The last two values correspond, respectively, to the shallowest and deepest sites where the March 2013 earthquake was recorded. The thickness of the three layers in the underlying crust remain unchanged, and the total thickness of the mesh becomes, respectively, 10.640 and 12.430 km.

The source is located 6 km below the maximal depth of the ocean (i.e., 9 km below the sea surface when $h = 3000$ m). The source time-function is a Gaussian signal with two possible dominant frequencies: 1 and 10 Hz. The resulting vertical velocity at the source is shown in Fig. 4 (bottom) both in the time-domain and in the frequency-domain for the 1 Hz dominant frequency. For the 10 Hz dominant frequency, the time-function and spectrum can be easily deduced by dividing the timescale by 10 and by multiplying the frequency scale by 10. The focal mechanism used is a pure shear, emitting both P and S waves,

$$\begin{pmatrix} -1 & 0 \\ 0 & 1 \end{pmatrix}_{(x,z)} \times 4.10^{16}\,\mathrm{N\,m}. \tag{3}$$

The selected seismic moment corresponds to a medium magnitude earthquake ($M_w = 5.0$), comparable to the one presented in Sec. IV.

The calculation domain is meshed according to the speeds of propagation of the waves in both media and to the frequency content ($\lesssim 25$ Hz, Fig. 4, bottom) of the signal to get finite elements with a typical size equal to half the shortest propagating wavelength ($\sim$60 m in the fluid medium and $\sim$ 120 m in the solid medium) (Cristini and Komatitsch, 2012). Using the SPECFEM2D internal mesher, the resulting mesh has 10 193 horizontal elements, 105 vertical elements in the crust, and 93 in the ocean. The whole mesh is thus made of 2 018 214 elements, where the minimum number of points per wavelength is 5.5 and the maximum frequency resolved, computed by SPECFEM2D, is 27.3 Hz. The typical run-time for a simulation is on the order of 13 h for 336 Intel Broadwell E5–2680 v4 2.4 GHz processors (Intel, Santa Clara, CA) grouped in 12 cores, with a 600 s long waveform calculated using a second order Newmark scheme and 1 500 000 time steps of $4{\cdot}10^{-4}$ s, which ensures the stability of the mesh for the considered element sizes and wave speeds. Though less time consuming than higher-order schemes the second order Newmark scheme can introduce additional numerical dispersion, along with the line source created by the 2D configuration.

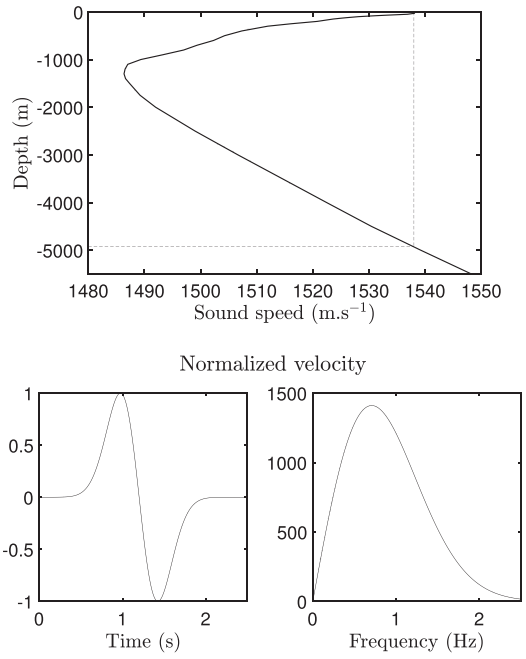

FIG. 4. (Top) sound-speed profile in the water column (solid line). The vertical dashed line shows the sound speed at the sea surface (1538 m s^{-1}) and the horizontal dashed line the critical depth (–4952 m). (Bottom) Signature of the 1 Hz-source seen in the time-domain (left) and in the frequency-domain (right).

B. Homogeneous ocean and crust

The seismo-acoustic waves produced in Configuration 2 with a 1 Hz source can be visualized in vertical snapshots of normalized pressure in the ocean and minus a third of the trace of the stress tensor in the crust (Fig. 5). The choice of this frequency prevents the incorrect visualization of short-wavelength waves. The animation in supplementary material provides a more intuitive and complete visualization of the wave propagation.[1] At $t = 6$ s, the P-wave propagating in the seafloor is visible as a vertical disturbance at $x = 26$ km, comprising a part with a negative polarity followed by a part with a positive polarity. The P wave generates a faded refracted wave in the ocean with a propagation angle equal to the critical vertical angle for total reflection from the seafloor, which is bounded on the surface of the ocean at $x = 16.5$ km. The refracted S wave is more intense, starting from the seafloor at $x = 15$ km and reaching the sea surface at $x = 10$ km, with a propagation front closer to the vertical, due to the lesser speed contrast between c_S and c_w. The

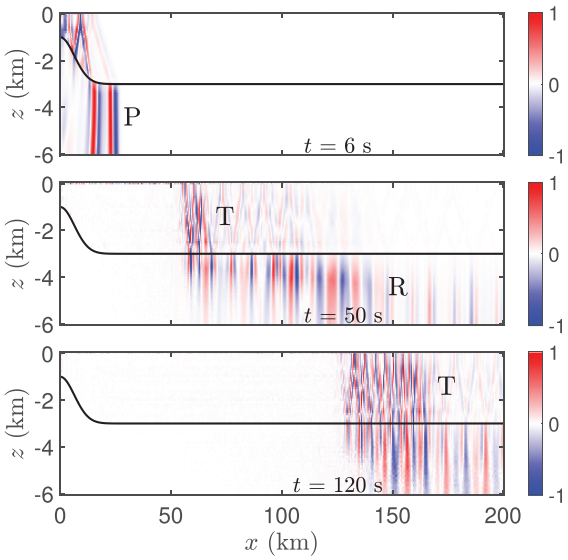

FIG. 5. (Color online) Snapshots of the acoustic pressure above and below the seafloor (black line), normalized by their maximum at each (x,z) point, at 6, 50, and 120 s since the beginning of the simulation (Configuration 2 with a 1 Hz-source). In the solid medium, the "pressure" is actually minus the third of the trace of the stress tensor. Capital letters denote the arrival fronts of P waves (P), precursory waves with a speed equal to c_R (R) and T waves (T).

energy of these multiple reflected refracted waves is concentrated on the top of the seamount. At $t = 50$ s, multiple reflections of the P wave on the sea surface are still visible in the crust, while the refracted wave is almost totally attenuated. The most intense waves in the crust are modes with frequencies below the Airy phase, with an arrival front at $x = 140$ km. The dispersive nature of these waves is shown by longer wavelengths arriving before shorter wavelengths. They are also visible in the ocean. Intense T waves are visible with an arrival front at $x = 70$ km. The snapshot at $t = 120$ s shows the widening of the T-wave train due to modal dispersion, after an arrival front at $x = 170$ km.

The waves generated by a 10 Hz-source in Configuration 1 can be easily identified in a time-distance diagram (Fig. 6, left), where the slope of the arrivals yields their speed. This diagram is built from the pressure time-series extracted along a 400 km-long horizontal antenna, with a hydrophone every 25 m, 1500 m below the sea surface. The pressure is normalized by its maximum at each hydrophone to compensate for the effect of the geometrical attenuation. The first arrival, at a speed $c_P = 5000\ \mathrm{m\,s^{-1}}$, are refracted waves due to the conversion of P waves into acoustic waves at the sea bottom, in the vicinity of each hydrophone. Note that the color bar must be saturated to make the refracted waves visible due to the difference in amplitude with the second arrival of acoustic T waves, at a speed $c_w = 1500\ \mathrm{m\,s^{-1}}$.

A 2D-Fourier transform will turn the time-distance diagram into a frequency-wavenumber diagram where the dispersion curves of the seismo-acoustic waves appear (Fig. 6, center). Modes are visible for phase speeds from c_S to a speed slightly higher than c_w ($\sim 1570\ \mathrm{m\,s^{-1}}$). They are energetic up to 25 Hz, both for phase speeds above and below c_R (i.e., below and above the Airy phase). The comparison at frequencies below 2.5 Hz and wavenumbers below $8\ \mathrm{m^{-1}}$ show a good agreement with the dispersion curves of the theoretical modes derived from Eq. (1) (Fig. 6, right). This conclusion stands for frequencies up to 25 Hz, but the resulting figure would be crowded.[1]

For a comparison with real data shown in Sec. IV, we focus the rest of Sec. III on the pressure waveform extracted at a hydrophone located 400 km away from the source, at mid-water depth. In the absence of intrinsic attenuation in the crust and with a source with a dominant frequency of 10 Hz (Configuration 1), the waveform shows a first arrival of refracted P waves at $t = 81$ s (Fig. 7, bottom). The second arrival at 285 s, much more prominent, corresponds to T waves, which reach their maximum amplitude at 315 s. The amplitudes drop abruptly after 427 s, but a coda lasts until at least 480 s. The spectrogram of this time signal shows that the arrival of T waves is preceded by the arrival of 15 low-amplitude modes below the Airy phase (Fig. 7, top). As modes are not energetic for phase velocities below $1570\ \mathrm{m\,s^{-1}}$ (Fig. 6 center), the part of the modes below the Airy phase is hidden by the part above the Airy phase at a frequency of 4.8 Hz, instead of the frequency of 3.9 Hz predicted from Fig. 2. Modes are energetic up to 25 Hz, both above and below the Airy phase, even if for frequencies above 5 Hz and arrival time between 285 and 307 s, the modal structure looks blurred. This is probably due to the limited time-resolution of the spectrogram, in a region

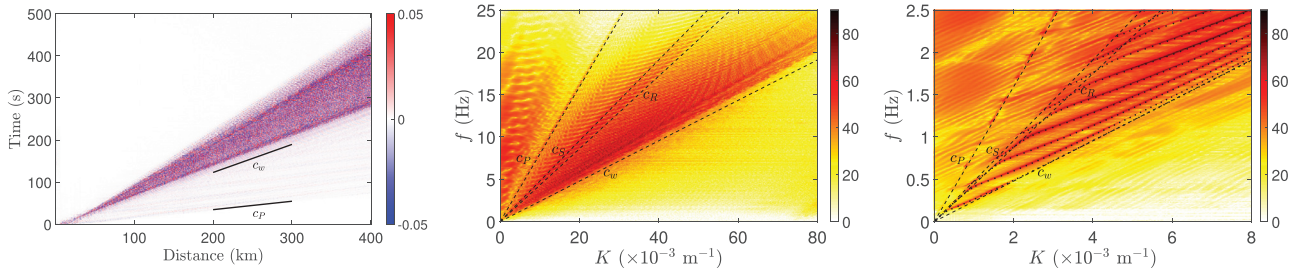

FIG. 6. (Color online) (Left) Time-distance diagram of the acoustic pressure normalized by its maximum at each hydrophone 1500 m below the sea surface, with no intrinsic attenuation in the crust (Configuration 1) and a source with a dominant frequency of 10 Hz. (Center) Frequency-wavenumber diagram of the normalized acoustic pressure showing the dispersion curves of simulated acoustic waves (color map). Black dashed lines show the phase speed of sound in water (c_w), Rayleigh waves (c_R), S waves (c_S), and P waves (c_P). (Right) Close-up of the middle figure showing the theoretical modes (black dotted curves) matching the dispersion curves of simulated acoustic waves.

https://doi.org/10.1121/10.0010529

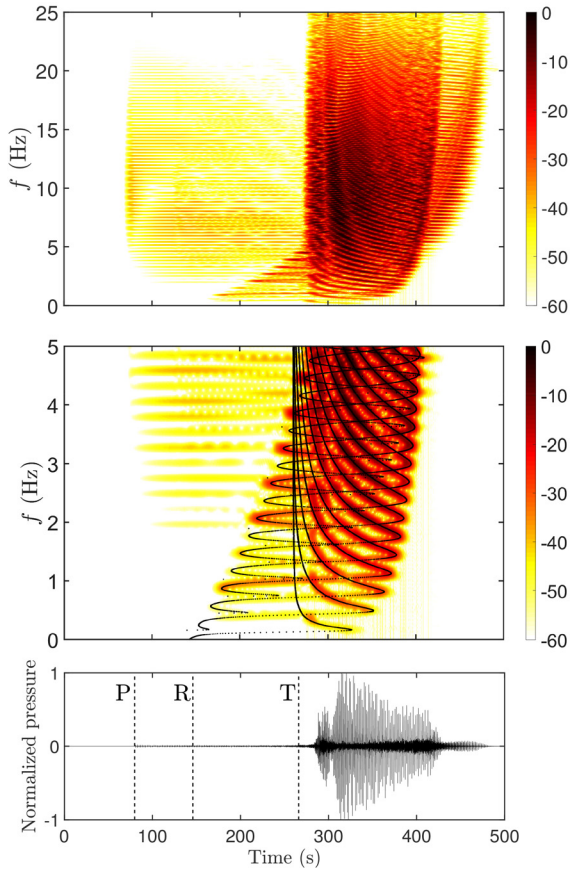

FIG. 7. (Color online) (Top) Spectrogram of pressure in dB re 1 Pa Hz$^{-1/2}$, 400 km away from the source and 1500 m below the sea surface, with no intrinsic attenuation in the crust (Configuration 1) and a source with a dominant frequency of 10 Hz (color map). (Center) Close-up of the spectrogram between 0 and 5 Hz with the theoretical arrival times of modes (black dots). (Bottom) Waveform; dashed lines annotated by capital letters show the arrivals of P waves (P), precursory waves with a speed equal to c_R (R), and T waves (T).

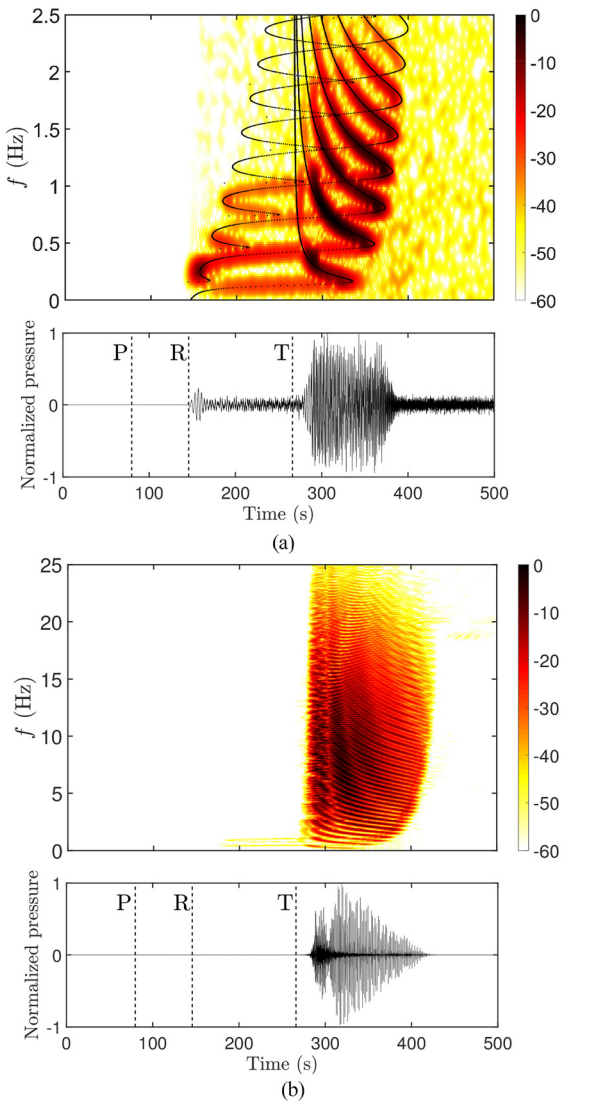

FIG. 8. (Color online) Spectrograms in dB re 1 Pa Hz$^{-1/2}$ (top) and waveform (bottom) of the pressure, 400 km away from the source and 1500 m below the sea surface with intrinsic attenuation in the crust (Configuration 2) and a source with a dominant frequency of 1 Hz (a) and 10 Hz (b). The dashed lines annotated by the capital letters show the arrivals of P waves (P), precursory waves with a speed equal to c_R (R), and T waves (T).

where modes with group speeds tending to c_w are not well separated. For frequencies above 4.5 Hz, the minimum of the group speeds just above the cut-off frequency is slower than the Airy phase, which explains the coda that follows T waves. A close up of the spectrogram for frequencies below 5 Hz (Fig. 7, center) compared to the theoretical arrival times, obtained by dividing the distance from the source by the theoretical group speeds shown in Fig. 2, demonstrates once again the good agreement of simulated modes with theoretical modes.

Adding intrinsic attenuation in the solid crust (Configuration 2) provides a more realistic view of the relative amplitude of the different waves expected in real signals, and how this amplitude varies with the frequency of the source. The resulting spectrograms for the two source-frequencies (1 and 10 Hz), only show a few modes energetic below the Airy phase, for frequencies below 2 Hz (Fig. 8). As a result, the coda due to modes below the Airy phase, above 4.5 Hz, observed in Fig. 7, vanishes. The intrinsic attenuation in the solid crust also causes the refracted P waves to disappear. Whereas the maximal frequency of modes below the Airy phase is roughly the same for the two source-frequencies, the maximum frequency of acoustic waves increases with the frequency of the source. For this reason, the relative amplitude of precursory waves decreases with increasing source frequency. With a source frequency of 1 Hz, they are clearly visible in the waveform, with a particularly intense arrival due to mode 2 [Fig. 8(a)]. At 10 Hz, these waves are barely visible and only in the spectrogram [Fig. 8(b)]. As the speed of the precursory waves decreases with increasing mode order, the length of the T-wave signal increases with increasing source frequency.

C. Inhomogeneous ocean and crust

Although unrealistic, the hypothesis of a homogeneous ocean and crust is useful to derive the theoretical speeds of modes (Sec. II) and to show that SPECFEM2D can be used

with confidence, given the consistency of the speeds of simulated modes with theoretical speeds (Sec. III B). We now use SPECFEM2D to predict modes in a configuration with a velocity-layered crust and a SOFAR channel in the ocean. As the main purpose of this section is to facilitate the interpretation of actual recordings of very low-frequency signals (Sec. IV), we restrict the simulations to a source frequency of 1 Hz, even if the effect of a SOFAR channel would be certainly more important at higher frequencies.

In the case of a three-layered crust with the densities and wave speeds listed in Table II, covered by a homogeneous ocean, the pressure signal at mid-depth, 400 km away from the source [Fig. 9(a), bottom), shows three distinct arrivals: refracted P waves at 65 s after the beginning of the simulation, precursory waves at 114 s and T waves at 285 s. The spectrogram [Fig. 9(a), top] contrasts with that for a homogeneous crust [Fig. 8(a), top]; the refracted P wave is particularly visible as a bright spot at about 65 s and a frequency near 0.2 Hz. Mode 0 and mode 1 are energetic below the Airy phase and mode 0 to 5 are energetic above the Airy phase. To check the agreement of these modes with the theoretical modes, we need to recalculate the theoretical group speeds. Of the six constant parameters in Eq. (1), $h = 3000$ m, $c_w = 1500\,\mathrm{m\,s^{-1}}$, and $\rho_w = 1000\,\mathrm{kg\,m^{-3}}$ are known and ρ_s can be taken equal to $3200\,\mathrm{kg\,m^{-3}}$ without disadvantages, which leaves the unknown c_P and c_S resulting from the three-layered crust (Table II). We can derive these unknowns by calculating c_P^{eff} and c_R^{eff}, the effective speeds of P waves and Rayleigh waves, from their arrival times (respectively, 65 and 114 s) and from the 400 km distance from the source. The effective speeds $c_P^{eff} = 6154\,\mathrm{m\,s^{-1}}$ and $c_R^{eff} = 3509\,\mathrm{m\,s^{-1}}$ are then used to obtain the effective speed of S waves $c_S^{eff} = 3869\,\mathrm{m\,s^{-1}}$ by inverting numerically the analytical approximation of the speed of Rayleigh waves (Viktorov, 1967),

$$c_R = c_S \frac{0.87 + 1.12\nu}{1+\nu}, \quad \nu = \frac{1}{2}\left[1 - \frac{1}{(c_P/c_S)^2 - 1}\right], \tag{4}$$

with ν being the Poisson ratio. The speeds of the modes calculated using $c_P^{eff} = 6154\,\mathrm{m\,s^{-1}}$ and $c_S^{eff} = 3869\,\mathrm{m\,s^{-1}}$ are used to obtain the theoretical arrival times shown as black dots in Fig. 9(a) (top). Given the limited time and frequency resolution of the spectrograms, these arrival times are in good agreement with the arrival times of simulated modes. We do not pretend that this method provides the best estimates of the arrival times, but it is simple and robust enough to be applied to real data without the computational costs of a proper geoacoustic inversion. Note that refracted P waves and the modes of interest are not the only visible waves in the spectrogram shown in Fig. 9(a) (top), which certainly also displays resonances within the two top layers of the crust, but these waves are out of the scope of this study.

In a model with a 3000 m deep ocean,1 we observed very few effects on the sound speed profile (Fig. 4) compared to an ocean layer with a constant sound speed [Fig. 9(a)]. Nonetheless, we consider here the most realistic case with a three-layered crust underlying an ocean with a SOFAR channel, with two different water depths: 3640 and 5430 m. The theoretical arrival times calculated with $c_P^{eff} = 6154\,\mathrm{m\,s^{-1}}$, $c_S^{eff} = 3869\,\mathrm{m\,s^{-1}}$, $c_w = 1500\,\mathrm{m\,s^{-1}}$, and, respectively, $h = 3640$ m [Fig. 9(b)] and $h = 5430$ m [Fig. 9(c)] are superimposed on the spectrograms of the resulting pressure waveforms. The pressure is extracted at mid-depth (respectively, –1820 and –2715 m) to separate the effect of the SOFAR channel from the effect of modal composition changing with depth. In both cases, the energetic arrivals of the simulated modes match the theoretical curves of arrival times, even though these curves assume a constant sound speed. The effect of the SOFAR channel is not null, as the modes are energetic for lower frequencies (and longer arrival times) for a deeper ocean, but it does not modify the dispersion curves in the tested range of depths. This absence of any noticeable effect may be due to the limited sensitivity of the speed of modes to the sound speed in a realistic range of values (Fig. 3); it may also be due to the limited time and frequency resolutions of the spectrograms. In any case, the

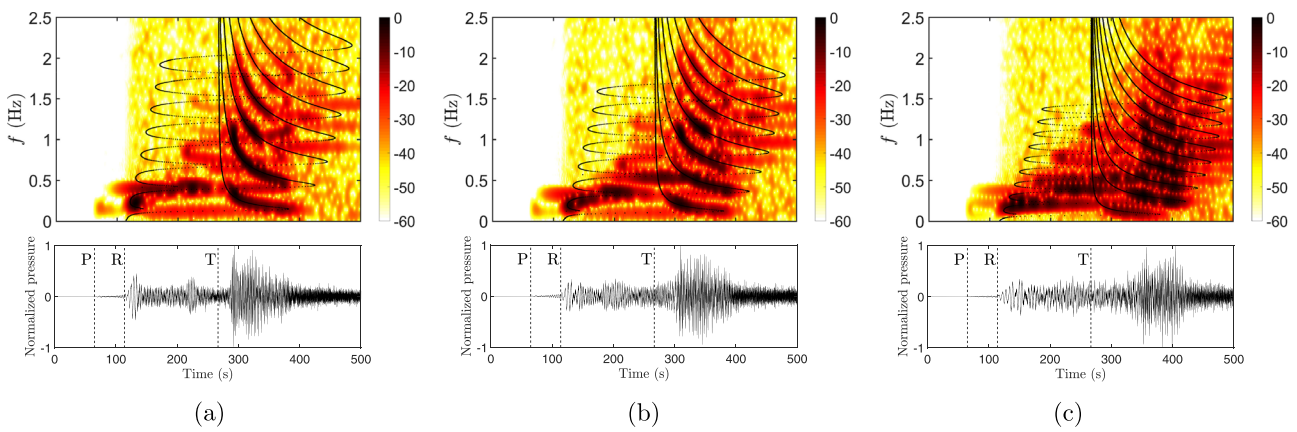

FIG. 9. (Color online) Spectrograms in dB re 1 Pa Hz$^{-1/2}$ (top) and waveforms (bottom) of the pressure, 400 km away from the source and at mid-depth with intrinsic attenuation in a three-layered crust, a source with a dominant frequency of 1 Hz, and a 3000 m-deep homogeneous ocean (Configuration 3) (a), a 3640 m-deep (Configuration 4b) (b), and 5430 m-deep (Configuration 4c) (c) ocean with a SOFAR channel. The dash lines annotated by the capital letters show the arrivals of P waves (P), precursory waves with a speed equal to c_R (R), and T waves (T).

https://doi.org/10.1121/10.0010529

theoretical modes prove to be relevant to predicting the arrival times of simulated modes even with a layered crust and a SOFAR channel in the ocean.

IV. REAL CASE

On March 15, 2013, at 9 h 46 m 45.6 s GMT, an intra-oceanic earthquake occurred near the axis of the Southeast Indian Ridge. The location of its epicenter (26°1′48″ S; 70°47′24″ E) and its magnitude ($M_w = 4.9$) were determined from land-based seismic stations (Global CMT, 2018). The propagating waves generated by this earthquake in the crust and the water column are well visible on recordings of eight ocean bottom seismometers (OBSs) from the RHUM-RUM experiment (Barruol and Sigloch, 2013). The data, freely accessible online (Network YV, 2011), were corrected from the instrument response (Stähler *et al.*, 2016). One of these OBSs was only 97 km away from the epicenter, near the Rodrigues Triple Junction (RR50) and the seven others were located along the Southwest Indian Ridge, with one of them at 227 km from the epicenter (RR49) and six in the SWIR array, at about 500 km from the epicenter (RR48, RR47, RR46, RR44, RR43, and RR41) (Fig. 10). The epicenter and all OBSs were near the ridge axis where the young oceanic crust is bare, i.e., the layer of pelagic sediment is only 10 m-thick (Divins, 2003).

The OBSs RR50 and RR49 are too close to the epicenter to record a clear separation of propagating waves, but three distinct arrivals are visible on waveforms from the SWIR array. In the rest of this article, we focus on vertical speed recorded by RR48, but the waveforms observed by the five other stations of the SWIR array are very similar and equally support our conclusions.[1] A first arrival is visible 69.4 s after the earthquake; a second more energetic arrival occurred 133.4 s after the earthquake; and a last one, energetic up to 35 Hz, 345.5 s after the earthquake (Fig. 11). If we make the hypothesis that recorded waves were emitted from the epicenter, 511 km away from RR48, at 9 h 46 m 45.6 s GMT, the mean speeds of the three propagating

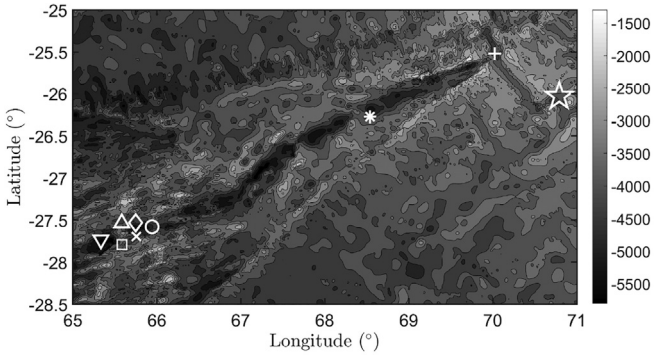

FIG. 10. Bathymetric chart of the western Indian Ocean with depth in meters showing the location of the March 15, 2013, earthquake epicenter (white star) and of the OBS stations from the RHUM-RUM experiment: RR50 (plus sign), RR49 (asterisk), RR48 (circle), RR47 (cross), RR46 (square), RR44 (diamond), RR43 (upward-pointing triangle), and RR41 (downward-pointing triangle). Isobaths are contoured every 500 m.

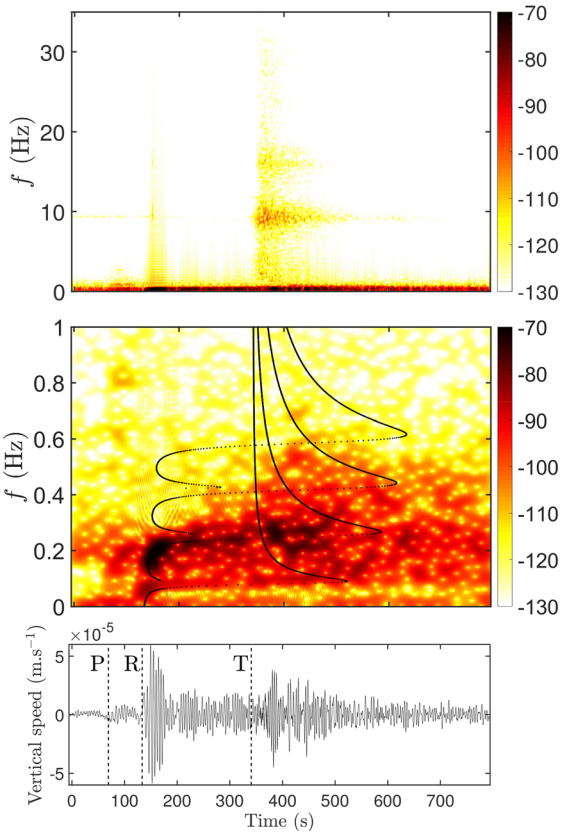

FIG. 11. (Color online) (Top) Spectrogram of the vertical component of OBS RR48 of the waveform generated by the March 15, 2013, earthquake in dB re 1 m s^{-1} Hz$^{-1/2}$ (color map). The OBS is located 511 km away from the epicenter. (Center) Close up of the spectrogram for frequencies below 1 Hz (color map) with the predicted arrival times of modes according to the frequency (black dots). (Bottom) Waveform high-pass filtered at 0.01 Hz. Dashed lines annotated by capital letters show the arrivals of P waves (P) at 69.4 s, precursory waves with a speed equal to c_R (R) at 133.4 s and T waves (T) at 345.5 s. Arrival times are based on the spectrogram.

waves are, respectively, 7362, 3830, and 1479 m s^{-1}. Such speeds match the expected speeds for as P waves, the predicted precursory waves and T waves.

For frequencies between 5 and 35 Hz, the spectrogram of the waveform does not show the dispersion curves expected if T waves propagate as modes (Fig. 11, top). However, the close up for frequencies below 1 Hz (Fig. 11, center) is qualitatively similar to the spectrograms from simulated pressure with an inhomogeneous crust (Fig. 9, top). The P-wave arrival is well outlined by a bright spot at times between 69 and 120 s and frequencies between 0.1 and 0.2 Hz. The most energetic arrivals preceding T waves seem to follow the arrival times of the theoretical mode 0 and mode 1. As a check, we calculated the arrival times of modes using the same method as for the simulations with an inhomogeneous crust (Sec. III C): we considered the effective speed of P waves deduced from observed arrival times ($c_P^{eff} = 7362$ m s^{-1}) and the effective speed of S waves ($c_S^{eff} = 4151$ m s^{-1}), obtained from c_P^{eff} and $c_R^{eff} = 3830$ m s^{-1} by inverting numerically Eq. (4). Other parameters used are the local depth at RR48, $h = 4830$ m (Stähler *et al.*, 2016), the crust density $\rho_s = 3200$ kg m^{-3}, and the nominal speed of

sound in water $c_w = 1500\,\mathrm{m\,s^{-1}}$, which was shown to be usable with the sound speed profile expected in March in this area (Sec. III C).

The predicted arrival times of modes are superimposed on the spectrogram (Fig. 11, center). The predicted mode 1 is in good agreement with the most energetic arrivals, between 135 and 340 s. However, if the shape of the observed mode 0 is very similar to that predicted, its frequency is about 0.02 Hz higher over the whole interval where it is visible (between 135 and 465 s). Such frequency offset for only one of the two well-visible modes is difficult to explain; either one of the parameters used to predict the arrival times has been poorly estimated or an effect has been overlooked in the derivation assumptions of the theoretical modes, for instance, the presence of a sediment layer. If we admit that the energy for frequencies between 0.15 and 0.30 Hz and times between 360 and 430 s can be interpreted in terms of modes, it could correspond to the part of a delayed mode 0 above the Airy phase, perhaps due to 3D effects in this hilly area.

V. DISCUSSION AND CONCLUSION

This paper first discusses the properties of modes in a fluid-solid waveguide and the ultra-low-frequency waves expected to precede T waves if they propagate as such modes. We then study the sensitivity of the group speeds of modes (which determine their arrival times) to five parameters of influence: the water depth, the speed of sound in the ocean, the speeds of P an S waves in the crust, and the ratio of densities. Although cursory, this study can be used as a first guide to apply theoretical modes to real environments with uncertainties in these parameters.

Second, SPECFEM2D simulations show that seismo-acoustic waves propagating in a homogeneous ocean above a homogeneous crust with no attenuation match the theoretical arrival times of modes. T waves and their precursors are energetic up to 25 Hz, the maximal frequency imposed by the simulated seismic source. With attenuation in the crust, the good agreement with the arrival times of theoretical modes remains, but only a few modes are energetic below the Airy phase, in the part conveying the ultra-low-frequency precursors of T waves. A simulation with a three-layered crust and a homogeneous ocean shows that theoretical modes calculated with constant speed values deduced from the arrival times of P waves and of the precursor of T waves are in good agreement with the simulated modes. Simulations with a three-layered crust and a realistic sound-speed profile in the ocean for three different water depths show that modes still follow the dispersion curves calculated with a constant sound speed, even if the distribution of the energy changes.

Finally, this paper presents a waveform recorded by an OBS showing seismo-acoustic waves generated by an earthquake. This waveform includes T waves energetic up to 35 Hz preceded by P waves and the expected ultra-low-frequency precursor. On its spectrogram, although T waves do not show the expected dispersion curves, they are preceded by two energetic regions resembling the theoretical modes. The arrival times of modes originating from the epicenter are calculated using the speeds of P and S waves, deduced from the observed arrival times of P waves and of the precursor of T waves, and the nominal speed of sound. The observed mode 1 is in good agreement with the predicted arrival times, but mode 0 shows an offset in frequency that could be explained by parameters not taken into account, for example, the presence of a very thin sediment layer. The signature of the selected earthquake may also reflect 3D effects in the propagation of waves and the lack of horizontal invariance of the waveguide, which distinguishes this real case from the simplified numerical models in Sec. III.

This paper provides indicative results on the presence of ultra-low-frequency waves propagating as modes and preceding T waves, but cannot bring new evidence of the modal behavior of T waves. With the high seismicity in the area of the RHUM-RUM experiment and the lack of a thick sediment layer, the large OBS array is ideal to search for complementary evidence. Waveforms from seismic events, recorded close enough to the epicenters so that the precursor of T waves is not completely attenuated, should be systematically analyzed for modes similar to those shown here, but with a signature closer to those simulated. Proofs may also come from T-wave records with banded structure in their spectrograms, similar to that presented by Butler and Lomnitz (2002). So the key of the demonstration relies on finding real data with low noise-levels and a modal structure not too affected by the lack of horizontal invariance in the actual waveguide. SPECFEM modeling applied to the real case could help to understand the differences between the theoretical dispersion curves and the ones observed in this complex environment. However, 3D modeling over such long distances would require very powerful numerical resources; furthermore, even 2D modeling would require considerable work on the crustal model to correctly reproduce seismic arrival times. Finally, the scope of this work could be broadened by taking into account a low-velocity sediment layer. The analytical developments already exist (e.g., Ardhuin *et al.*, 2013) and remain to be applied to T waves, tested through numerical modeling, and compared with real data.

ACKNOWLEDGMENTS

The SPECFEM2D code was run on Datarmor, a massive computing facility common to several research institutions at the western-most tip of Brittany. The authors are grateful to Charles Peureux and Fabrice Ardhuin for useful discussions on the theoretical modes, to Paul Cristini for his help on modeling media with varying parameters in SPECFEM2D and to the midshipmen Chové, du Cauze de Nazelle, Palfray Aubin de Jaurias and Vignol, whose student project led us to the fortuitous discovery of the seismic event presented in this article. The authors thank the Associate Editor Dr. Y.-T. Lin and three anonymous reviewers for their constructive and insightful comments on the original manuscript that greatly helped to improve the paper. Most of the work in this paper was carried out while

J.L. was supported by a joint Ph.D. fellowship from the *Délégation Générale à l'Armement (DGA)* and the Regional Council of Brittany (*Région Bretagne*).

[1]See supplementary material at https://www.scitation.org/doi/suppl/10.1121/10.0010529 for an animation showing the pressure normalized every 4 s by its maximum at each position in the *xz*-plan; a comparison between simulated and theoretical dispersion curves in a frequency-wavenumber diagram between 20 and 25 Hz; a comparison between the results obtained with a 3000 m deep ocean with a constant sound speed or with a sound-speed profile; waveforms and spectrograms from the stations RR50, RR49, RR48, RR47, RR46, RR44, RR43, and RR41, with modes arrival times added to the spectrograms and parameters used to calculate them.

Ardhuin, F., Lavanant, T., Obrebski, M., Mari, L., Royer, J.-Y., d'Eu, J.-F., Howe, B. M., Lukas, R., and Aucan, J. (**2013**). "A numerical model for ocean ultra-low frequency noise: Wave-generated acoustic-gravity and Rayleigh modes," J. Acoust. Soc. Am. **134**(4), 3242–3259.

Ball, J. S., Godin, O. A., Evers, L. G., and Lv, C. (**2016**). "Long-range correlations of microseism-band pressure fluctuations in the ocean," Geophys. J. Int. **206**(2), 825–834.

Barruol, G., and Sigloch, K. (**2013**). "Investigating La Réunion hot spot from crust to core," Eos. Trans. AGU. **94**(23), 205–207.

Bassin, C., Laske, G., and Masters, G. (**2000**). "The current limits of resolution for surface wave tomography in North America," EOS Trans. Am. Geophys. Union **81**, F897.

Biot, M. A. (**1952**). "The interaction of Rayleigh and Stoneley waves in the ocean bottom," Bull. Seism. Soc. Am **42**(1), 81–93.

Bottero, A. (**2018**). "Full-wave numerical simulation of t-waves and of moving acoustic source," Ph.D. thesis, Université Aix-Marseille, Marseille, France.

Butler, R., and Lomnitz, C. (**2002**). "Coupled seismoacoustic modes on the seafloor," Geophys. Res. Lett. **29**(10), 57-51–57-4, https://doi.org/10.1029/2002GL014722.

Chen, C. W., Huang, C. F., Lin, C. W., and Kuo, B. Y. (**2017**). "Hydroacoustic ray theory-based modeling of T wave propagation in the deep ocean basin offshore eastern Taiwan," Geophys. Res. Lett. **44**(10), 4799–4805, https://doi.org/10.1002/2017GL073516.

Cristini, P., and Komatitsch, D. (**2012**). "Some illustrative examples of the use of a spectral-element method in ocean acoustics," J. Acoust. Soc. Am. **131**(3), EL229–EL235.

de Groot-Hedlin, C. D., and Orcutt, J. A. (**1999**). "Synthesis of earthquake-generated T-waves," Geophys. Res. Lett. **26**(9), 1227–1230, https://doi.org/10.1029/1999GL900205.

de Groot-Hedlin, C. D., and Orcutt, J. A. (**2001**). "Excitation of T-phases by a seafloor scattering," J. Acoust. Soc. Am. **109**(5), 1944–1954.

Divins, D. L. (**2003**). *Total Sediment Thickness of the World's Oceans & Marginal Seas* (NOAA National Geophysical Data Center, Boulder, CO).

D'Spain, G. L., Berger, L. P., Kuperman, W. A., Stevens, J. L., and Baker, G. E. (**2001**). "Normal mode composition of earthquake T phases," Pure Appl. Geophys. **28**(13), 2537–2540.

Dushaw, B. (**2011**). "Worldwide sound speed, temperature, salinity, and buoyancy from the NOAA World Ocean Atlas," https://staff.washington.edu/dushaw/WOA/ (Last viewed March 3, 2022).

Dziak, R. P. (**2001**). "Empirical relationship of T-waves energy and fault parameters of northeast Pacific Ocean earthquakes," Geophys. Res. Lett. **28**(13), 2537–2540, https://doi.org/10.1029/2001GL012939.

Ewing, M., Jardetzky, W. S., and Press, F. (**1957**). *Elastic Waves in Layer Media* (McGraw-Hill, New York).

Ewing, M., Tolstoy, I., and Press, F. (**1950**). "Propose use of the T phase in tsunami warning systems," Bull. Seism. Soc. Am. **40**(1), 53–58.

Fox, C. G., Dziak, R. P., Matsumoto, H., and Schreiner, A. E. (**1994**). "Potential for monitoring low-level seismicity on the Juan de Fuca Ridge using military hydrophone arrays," Mar. Tech. Soc. J. **27**(4), 22–30.

Fox, C. G., Matsumoto, H., and Lau, T.-K. A. (**2001**). "Monitoring Pacific Ocean seismicity from an autonomous hydrophone array," J. Geophys. Res. **106**(B3), 4183–4206, https://doi.org/10.1029/2000JB900404.

Franck, S. D., Collis, J. M., and Odom, R. I. (**2015**). "Elastic parabolic equation solutions for oceanic T-waves generation and propagation from deep seismic sources," J. Acoust. Soc. Am. **137**, 3534–3543.

Global CMT (**2018**). "Global CMT Web Page," www.globalcmt.org (Last viewed May 10, 2022).

Jamet, G., Guennou, C., Guillon, L., Mazoyer, C., and Royer, J.-Y. (**2013**). "T-wave generation and propagation: A comparison between data and spectral element modeling," J. Acoust. Soc. Am. **134**(4), 3376–3385.

Johnson, R. H. (**1966**). "Routine location of T-phase sources in the Pacific," Bull. Seism. Soc. Am. **56**(1), 109–118.

Johnson, R. H., Norris, R. A., and Dunnebier, F. K. (**1968**). "Abyssal generated T phase," in *Crust Upper Mantle Pacific Area* (AGU, Washington, DC), Vol. 12.

Johnson, R. H., Northrop, J., and Eppley, R. (**1963**). "Source of Pacific T waves," J. Geophys. Res. **68**(14), 4251–4260, https://doi.org/10.1029/JZ068i014p04251.

Lecoulant, J., Guennou, C., Guillon, L., and Royer, J.-Y. (**2019**). "Three-dimensional-modeling of earthquake generated acoustic waves in the ocean in simplified configurations," J. Acoust. Soc. Am. **146**(3), 2113–2123.

Milne, A. R. (**1959**). "Comparison of spectra of an earthquake T phase with similar signals from nuclear explosions," Bull. Seism. Soc. Am. **49**(4), 317–329.

Network YV (**2011**). "Résif: Network YV (2011)," http://dx.doi.org/10.15778/RESIF.YV2011 (Last viewed May 10, 2022).

NOAA (**2015**). "WOA09: NOAA World Ocean Atlas 2009," https://www.nodc.noaa.gov/OC5/WOA09/pr_woa09.html (Last viewed March 3, 2022).

Officer, C. B. (**1958**). *Introduction to the Theory of Sound Transmission, with Application to the Ocean* (McGraw-Hill, New York).

Oliveira, T., and Lin, Y.-T. (**2019**). "Three-dimensional global scale underwater sound modeling: The T-phase wave propagation of a Southern Mid-Atlantic Ridge earthquake," J. Acoust. Soc. Am. **146**(3), 2124–2135.

Park, M., Odom, R. I., and Soukip, D. J. (**2001**). "Modal scattering: A key to understanding oceanic T-waves," Geophys. Res. Lett. **28**(17), 3401–3404.

Pekeris, C. L. (**1948**). "Theory of propagation of explosive sound in shallow water," Geol. Soc. Am. Mem. **27**(2), 117.

Piserchia, P.-F., Virieux, J., Rodrigues, D., Gaffet, S., and Talandier, J. (**1998**). "Hybrid numerical modelling of T-wave propagation: Application to the Midplate experiment," Geophys. J. Int. **133**(3), 789–800.

Porter, M. B. (**1991**). *The Kraken Normal Mode Program, User's Manual* (SACLANT Undersa Research Centre, La Spezia, Italy).

Press, F., Ewing, M., and Tolstoy, I. (**1950**). "The Airy phase of a shallow-focus submarine earthquake," Bull. Seism. Soc. Am. **40**(2), 111–148.

Schreiner, A. E., Fox, C. G., and Dziak, R. P. (**1995**). "Spectra and magnitudes of T-waves from the 1993 earthquake swarm on the Juan de Fuca Ridge," Geophys. Res. Lett. **22**(2), 139–142, https://doi.o10.1029/94GL01912.

Searle, R. (**2013**). *Mid-Ocean Ridges* (Cambridge University Press, Cambridge, UK).

Stähler, S. C., Silgoch, K., Hosseini, K., Crawford, W. C., Barruol, G., Schmidt-Aursch, M. C., Tsekhmistrenko, M., Scholz, J.-P., Mazzullo, A., and Deen, M. (**2016**). "Performance report of the RHUM-RUM ocean bottom seismometer network around La Réunion, western Indian Ocean," Adv. Geosci. **41**, 43–63.

Stevens, J. L., Hanson, J., Nielsen, P., Zampolli, M., Bras, R. L., Haralabus, G., and Day, S. M. (**2020**). "Calculation of hydroacoustic propagation and conversion to seismic phases at T-stations," Pure Appl. Geophys. **178**, 2579–2609.

Stoneley, R. (**1926**). "The effect of the ocean on Rayleigh waves," Mon. Not. R. Astron. Soc. Geophys. **1**(7), 349–356.

Talandier, J., and Okal, E. A. (**1998**). "On the mechanism of conversion of seismic waves to and from T waves in the vicinity of island shores," Bull. Seism. Soc. Am. **88**(2), 621–632.

Tolstoy, L., and Ewing, W. M. (**1950**). "The T phase of shallow-focus earthquakes," Bull. Seism. Soc. Am. **40**(2), 25–52.

Tromp, J., Komatitsch, D., and Qinya, L. (**2008**). "Spectral-element and adjoint methods in seismology," Commun. Comput. Phys. **3**(1), 1–32.

Viktorov, I. A. (**1967**). *Rayleigh and Lamb Waves Physical Theory and Applications* (Springer, New York).

Vinh, P. C. (**2013**). "Scholte-wave velocity formulae," Wave Motion **50**(2), 180–190.

Xie, Z., Matzen, R., Cristini, P., Komatitsch, D., and Martin, R. (**2016**). "A perfectly matched layer for fluid-solid problems: Application to ocean-acoustics simulations with solid ocean bottoms," J. Acoust. Soc. Am. **140**(1), 165–175.

Yang, Y., and Forsyth, D. W. (**2003**). "Improving epicentral and magnitude estimation of earthquakes from T-phases by considering the excitation function," Bull. Seism. Soc. Am. **93**(5), 2106–2122.